Chemical Science

ROYAL SOCIETY OF CHEMISTRY

EDGE ARTICLE

View Article Online
View Journal | View Issue

Cite this: *Chem. Sci.*, 2021, **12**, 11554

All publication charges for this article have been paid for by the Royal Society of Chemistry

Accurate heteronuclear distance measurements at all magic-angle spinning frequencies in solid-state NMR spectroscopy†

Lixin Liang,[ab] Yi Ji,[ab] Zhenchao Zhao,[a] Caitlin M. Quinn,[c] Xiuwen Han,[a] Xinhe Bao,[a] Tatyana Polenova[c] and Guangjin Hou*[a]

Received 12th June 2021
Accepted 20th July 2021

DOI: 10.1039/d1sc03194e

rsc.li/chemical-science

Heteronuclear dipolar coupling is indispensable in revealing vital information related to the molecular structure and dynamics, as well as intermolecular interactions in various solid materials. Although numerous approaches have been developed to selectively reintroduce heteronuclear dipolar coupling under MAS, most of them lack universality and can only be applied to limited spin systems. Herein, we introduce a new and robust technique dubbed phase modulated rotary resonance (PMRR) for reintroducing heteronuclear dipolar couplings while suppressing all other interactions under a broad range of MAS conditions. The standard PMRR requires the radiofrequency (RF) field strength of only twice the MAS frequency, can efficiently recouple the dipolar couplings with a large scaling factor of 0.50, and is robust to experimental imperfections. Moreover, the adjustable window modification of PMRR, dubbed wPMRR, can improve its performance remarkably, making it well suited for the accurate determination of dipolar couplings in various spin systems. The robust performance of such pulse sequences has been verified theoretically and experimentally *via* model compounds, at different MAS frequencies. The application of the PMRR technique was demonstrated on the H-ZSM-5 zeolite, where the interaction between the Brønsted acidic hydroxyl groups of H-ZSM-5 and the absorbed trimethylphosphine oxide (TMPO) were probed, revealing the detailed configuration of super acid sites.

Introduction

Dipolar interactions lie at the core of solid-state nuclear magnetic resonance (NMR) spectroscopy. In spin systems comprising multiple spins, the anisotropic heteronuclear dipolar interaction plays a crucial role in elucidating through-space correlations, and it is also profoundly sensitive to the motion of the spins involved.[1] Therefore, the knowledge of the accurate heteronuclear dipolar coupling constant (DCC) can provide significant information on the molecular structure and dynamics. However, the direct observation of heteronuclear dipolar interactions in static solids is often hindered by severe spectral overlap from multiple spins or complicated by homogeneous line broadening from multiple anisotropic NMR interactions. The advent of the magic-angle spinning (MAS) technique accelerated the rapid development of high-resolution solids-state NMR spectroscopy. In MAS, the sample is mechanically rotated at a judiciously chosen axis, the "magic angle", resulting in the averaging (over the rotor period) of anisotropic NMR spin interactions including heteronuclear dipolar couplings, and hence high spectral resolution.[2–8] This is accompanied by the loss of orientational information, which is directly linked to the structure and dynamics. To overcome this limitation, numerous approaches have been developed to selectively reintroduce dipolar couplings under MAS, generally termed dipolar recoupling. These usually are based on the application of rotor-synchronized periodic RF field irradiations.[9–14] Despite the usefulness of the currently available dipolar recoupling methods, most of them lack universality and are only suited for specific spin systems or under certain experimental conditions.

Rotary resonance recoupling (R^3) was first discovered by Oas and Levitt in 1988, and it occurs when the nutation frequency (ν_1) of the applied RF field matches the MAS frequency (ν_r) at $\nu_1 = n\nu_r$, ($n = 1$ or 2).[12,15] Under this condition, the heteronuclear dipolar interaction averaged by the MAS rotation can be restored, whereas the homonuclear dipolar interaction is reintroduced simultaneously for $n = 1$, or suppressed for $n = 2$. Although the R^3 method is easy to implement experimentally, it suffers from the lack of strict selectivity for recoupling and high sensitivity to rf mismatch or inhomogeneity,[12] limiting its

[a]State Key Laboratory of Catalysis, National Laboratory for Clean Energy, 2011-Collaborative Innovation Center of Chemistry for Energy Materials, Dalian Institute of Chemical Physics, Chinese Academy of Sciences, Zhongshan Road 457, Dalian 116023, China. E-mail: ghou@dicp.ac.cn

[b]University of Chinese Academy of Sciences, Beijing 100049, China

[c]Department of Chemistry and Biochemistry, University of Delaware, Newark, Delaware 19716, USA

† Electronic supplementary information (ESI) available. See DOI: 10.1039/d1sc03194e

practical applications. Rotational echo double resonance (REDOR) developed by Gullion and Schaefer is another widely used technique for measuring heteronuclear dipolar couplings;[13,16] therein the utilization of phase-cycled π pulses greatly improved the robustness to experimental imperfections.[17–22] However, the homonuclear dipolar interactions are partially reintroduced during REDOR irradiation, which causes the loss of accuracy in heteronuclear dipolar coupling measurements.[23] To obtain precise heteronuclear dipolar recoupling with more restrictive selections, the *R*-symmetry concept has been applied for the design of pulse sequences suited for H–X dipolar measurements in fully protonated systems.[14,24–27] *R*-Symmetry sequences can be used for the accurate determination of heteronuclear dipolar couplings in a wide range of RF fields and MAS frequencies. While more versatile than most other approaches, these sequences suffer from the generally low scaling factor, interference from the chemical shift anisotropy (CSA) interaction and sensitivity to RF mismatch.[27] Some improvements have been made in recent years to the basic *R*-symmetry dipolar recoupling, such as the phase alternating *R*-symmetry (PARS) scheme[28] and windowed PARS with composite pulses of $90^{\circ}_{x} - \tau - 90^{\circ}_{x}$,[29] but the complexity of these recoupling sequences limits their widespread applications. Alternatively, the phase cycled $R4^2_1$ symmetry sequence, dubbed SR4,[30–32] was introduced for heteronuclear dipolar determination, where interference of CSA and dipolar truncation can be avoided. According to symmetry theory, the homonuclear dipolar and chemical shift interactions are also symmetry-allowed by $R4^2_1$, but suppressed efficiently by the utilization of $[R4^2_1\, R4^{-2}_1]$ phase cycling. SR4 with relatively low RF requirement of $\nu_1 = 2\nu_r$ is particularly suitable for fast MAS conditions. However, the low RF requirement hampers its robustness to resonance offset and homonuclear dipolar interactions, which becomes more pronounced under slow-to-moderate MAS conditions.

Here we present a new robust heteronuclear recoupling sequence, dubbed phase-modulated rotary resonance (PMRR). The PMRR recoupling sequence with an adjustable RF field strength of $\geq 2\nu_r$ allows for accurate measurement of dipolar coupling in a broad range of spinning frequencies from slow to ultrafast MAS. Benefiting from the original R^3 at $n = 2$, the PMRR method has several advantages: (i) high recoupling efficiency with a scaling factor ≥ 0.50, (ii) efficient suppression of homonuclear dipolar interactions, and (iii) straightforward set up. More importantly, the introduction of phase modulation significantly improves the robustness to RF mismatch (or inhomogeneity), interference from CSA and resonance offset. With window modification on the PMRR scheme, the scaling factor can be further improved from 0.50 to over 0.60, and the robustness to the undesired interferences can be further boosted. The performance of heteronuclear (H–X or X–Y) dipolar recoupling by PMRR sequences has been evaluated numerically and experimentally in U–^{13}C, ^{15}N–fMLF and U–^{13}C, ^{15}N–histidine·H_2O·HCl at different MAS frequencies. An application by proton-detected PMRR is then demonstrated in a practical zeolite sample to measure the inter-atomic distance between the ^{31}P of adsorbed TMPO and ^{1}H of Brønsted acids in the zeolite.

Experimental

Sample preparation

The standard sample, U–^{13}C, ^{15}N–fMLF was purchased from Giotto Biotech and packed in 3.2 mm and 1.3 mm zirconia rotors. The H-ZSM-5 ($SiO_2/Al_2O_3 = 23$) zeolite was obtained by calcining the NH_4-form zeolite (CBV2314 from Zeolyst International) at 823 K for 4 h in a furnace. Before the adsorption of TMPO, H-ZSM-5 was dehydrated under vacuum ($<10^{-3}$ Pa) at 693 K for 12 h. A given amount of TMPO (3 mg TMPO per 100 mg zeolite) dissolved in anhydrous CH_2Cl_2 was added into a sealed vessel containing the dehydrated sample in a N_2 atmosphere. The loaded sample was stilled at room temperature for at least 24 h and then evacuated on a vacuum line at 323 K for 1 h to remove CH_2Cl_2. The sample was further heated at 443 K for 1 h to guarantee uniform adsorption of the TMPO molecules. Finally, the sample was transferred into a 3.2 mm zirconia rotor in the Ar glove box.

Solid-state NMR experiments

The NMR experiments of U–^{13}C, ^{15}N–fMLF and histidine were performed on three Bruker NMR spectrometers, wide-bore 14.10 T AVIII 600 with a 3.2 mm HXY probe at 16 kHz MAS, standard-bore 18.18 T AV NEO 800 with a 1.3 mm HX probe at 60 kHz MAS, and standard-bore 19.97 T AVIII HD 850 with a 1.3 mm HCN probe at 60 kHz MAS. The experiments of the TMPO adsorbed H-ZSM-5 zeolite were conducted on the AVIII 600 spectrometer, operating with a 3.2 mm HXY probe at 20 kHz MAS. In the pulse sequences shown below, narrow white rectangles represent 90° pulses; grey rectangles are 180° pulses, unless specified otherwise.

1D ^{31}P NMR spectra were acquired by ^{1}H–^{31}P CP with 5.0 ms contact time at a MAS frequency of 20 kHz. In 2D ^{31}P–^{1}H HETCOR spectra, $128t_1$ increments in the indirect dimension (F1) were recorded with 16 scans and a recycle delay of 2 s. For the 3D ^{31}P/^{1}H–^{31}P/^{1}H correlation NMR experiment, the ^{1}H 90° pulse length was 2.82 μs, and the first and second ^{1}H–^{31}P CP conditions are the same with experimentally optimized RF fields matching the first-order Hartmann–Hahn conditions. ^{1}H SPINAL decoupling with a RF field strength of 88.7 kHz was applied during the t_1 dimension. The RF amplitude of windowed PMRR-REDOR ($f_w = 0.55$) recoupling was 88.7 kHz.

Simulations

Numerical simulations were performed on the SIMPSON v2.0 software, with rep320 as the crystal file and 64 γ-angles for powder averaging. The B_0 field was 14.10 T (600 MHz ^{1}H Larmor frequency), and the MAS frequency ranged from 10 kHz to 120 kHz. RF mismatch and resonance offset were only set on the channel with the recoupling irradiation unless mentioned specifically.

Results and discussion

Phase modulated rotary resonance (PMRR)

As discussed elsewhere,[33,34] the R^3 scheme with a RF field of $2\nu_r$ can efficiently reintroduce the heteronuclear dipolar interaction while suppressing the first-order homonuclear dipolar interaction. However, due to its inherent characteristics, including non-strict selectivity, as well as high sensitivity to resonance offset, pulse imperfection and RF inhomogeneity, its practical application is very limited despite the ease of experimental setup and a large scaling factor. To remove these limitations, we introduced phase modulation into the R^3 sequence, and called it the modified sequence phase-modulated rotary resonance (PMRR). The basic PMRR scheme entails continuous RF irradiation that satisfies the $n = 2$ rotary resonance condition ($\nu_1 = 2\nu_r$), whereas a 180° phase shift is applied every rotor period. A repetitive sequence block therefore lasts for two rotor cycles, denoted as $(4\pi)_x(4\pi)_{-x}$, as shown in Fig. 1a. Although the R^3 scheme involves continuous wave (CW) RF irradiation with a field strength of $2\nu_r$, it can be classified as the $R4_1^4$ (or $R4_1^0$) symmetry sequence.[35] According to the principle of the symmetry-based sequences,[24] the recoupled first-order dipolar Hamiltonian by R^3, denoted in (m, l, λ, μ) quantum numbers, contains zero-quantum (2, ±2, 1, 0) and single-quantum (2, ±2, 1, ±1) terms. The XiX two-step phase modulation in PMRR averages out single-quantum Hamiltonian terms, with only the zero-quantum terms (I_zS_z) remaining. Because of the identical symmetry properties, the CSA interaction is reintroduced simultaneously with the heteronuclear dipolar coupling. In the original R^3 sequence, this recoupled CSA interaction could interfere with heteronuclear dipolar couplings, thus hampering accurate dipolar coupling measurements (Fig. S1a†). On the other hand, in the PMRR sequence, the zero-quantum CSA terms (I_z) are simultaneously recoupled, but they are commutative with zero-quantum dipolar terms (I_zS_z), therefore producing negligible interference to the dipolar evolution.[14]

General 2D PMRR-based pulse sequences for heteronuclear dipolar measurements are shown in Fig. 1b and c, corresponding to either the conventional REDOR[13] or dipolar and chemical shift (DIPSHIFT)[36] schemes, respectively. PMRR-REDOR and PMRR-DIPSHIFT sequences recouple identical zero-quantum dipolar terms.[37] The spin echoes produced by the simultaneous π pulses of the PMRR-REDOR scheme in Fig. 1b refocus the chemical shift terms for both I and S spins, making

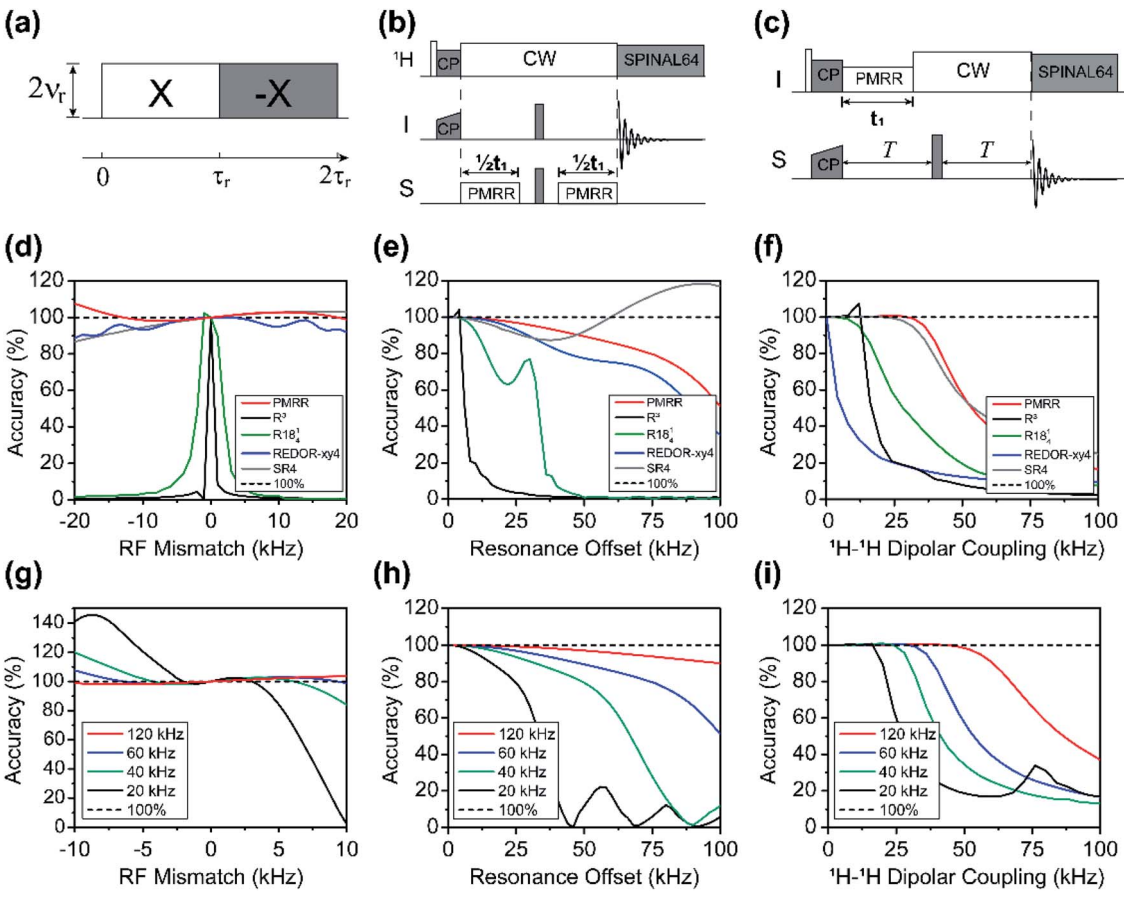

Fig. 1 (a) Basic PMRR block that consists of $n = 2$ rotary resonance modulated by rotor-synchronized 0, π phase cycle; 2D pulse sequences of PMRR-REDOR (b) and PMRR-DIPSHIFT (c). The robustness to (d) RF mismatch, (e) resonance offset and (f) ^{1}H–^{1}H dipolar coupling by PMRR (red), RR (black), R1841 (green), REDOR-xy4 (blue), and SR4 (grey) recoupling schemes at 14.1 T and a MAS rate of 60 kHz. The robustness to (g) RF mismatch, (h) resonance offset and (i) ^{1}H–^{1}H dipolar coupling by PMRR at MAS frequencies of 20 kHz (black), 40 kHz (green), 60 kHz (blue), and 120 kHz (red). The dashed lines indicate ideal cases.

the method insensitive to CSA and resonance offset. We note that both spins are suitable for observation in this experiment.[38] In contrast, in the PMRR-DIPSHIFT scheme (Fig. 1c), the chemical shift terms of spin S alone are refocused, making S the only observable channel. Since the zero-quantum CSA terms commute with the zero-quantum dipolar terms, the dipolar evolution generated by PMRR-DIPSHIFT is also insensitive to the CSA interaction, similar to PMRR-REDOR, as illustrated in Fig. S1b.† It should be noted that both PMRR-REDOR and PMRR-DIPSHIFT are affected by T_2 relaxation. The influence of T_2 decay in the REDOR-type scheme can be taken into account by conducting an additional control experiment (S_0) which omits all the pulses on the non-observed channel, and $\Delta S/S_0$ is often used to denote the dipolar evolution.[13] Alternatively, the influence of T_2 decay can be removed by using a constant echo time,[39] as shown in PMRR-DIPSHIFT (Fig. 1c). Inevitably, longer constant echo time results in more signal loss.

The small ratio of $\nu_1/\nu_r = 2$ makes PMRR suitable for fast-to-ultrafast MAS conditions, and it is expected that better performance would be achieved at a faster MAS frequency, mainly due to the higher applied RF field. We first evaluated the performance of the PMRR sequence at an ultrafast MAS frequency of 60 kHz by numerical simulations, and compared it to that of other commonly used recoupling approaches including R^3 REDOR, SR4, and single-quantum RN_n^{ν} sequences. The robustness of the recoupling sequences was evaluated for different conditions, including RF mismatch, resonance offset and ^{1}H–^{1}H dipolar coupling. The results are shown in Fig. 1d–f, respectively. The simulations clearly indicate that the original R^3 sequence is highly sensitive to the RF mismatch and resonance offset. For instance, a slight RF mismatch of 0.5 kHz results in over 50% error (Fig. 1d), and a 6.5 kHz resonance offset leads to an error of over 10% (Fig. 1e). Considering the similar RF field requirement of $2.25\nu_r$, $R18_4^1$ was selected for examining the performance of the single-quantum recoupling scheme at a MAS frequency of 60 kHz. As reported previously,[35] $R18_4^1$ with $\nu_1/\nu_r < 2.5$ is easily influenced by RF mismatch and resonance offset, but exhibits better tolerance than R^3, as shown in Fig. 1d and e. In comparison, the significantly improved robustness can be achieved by the PMRR scheme, and the phase modulation efficiently compensates for the influence from RF mismatch and resonance offset, which is similar to REDOR-xy4 and SR4. Under the given simulation condition, it is noted that PMRR shows slightly better tolerance than SR4 and REDOR (Fig. 1d and e). More specifically, by the PMRR recoupling scheme, even a large RF mismatch of up to ±10% only results in a minor deviation of less than 4%. Assuming that the allowable error of dipolar measurements is 10%, the tolerable resonance offsets are ±40, ±38.5 and ±21.5 kHz for PMRR, REDOR and SR4 schemes, respectively (Fig. 1e).

For practical applications of H–X dipolar coupling measurements, ^{1}H–^{1}H homonuclear dipolar decoupling is another major factor in evaluating the performance of recoupling sequences, except for proton dilute or deuterated systems.[23,40,41] Although REDOR is as robust as PMRR in terms of RF mismatch and resonance offset, REDOR suffers from the influence of simultaneously recoupled homonuclear dipolar interactions, as demonstrated in Fig. 1f. In contrast, in the R^3 ($n = 2$) and $R18_4^1$ sequences, homonuclear dipolar interactions are decoupled at MAS frequencies exceeding 40 kHz, due to the inherent averaging of the first-order homonuclear Hamiltonian terms. Surprisingly, the PMRR scheme exhibits greatly improved homonuclear dipolar decoupling compared to the original R^3 ($n = 2$), effectively suppressing the influence of ^{1}H–^{1}H dipolar couplings in the H–X dipolar coupling measurements. In addition, it should be noted that in SR4 homonuclear dipolar decoupling takes place *via* a supercycle over the $R4_1^2$ unit, although $R4_1^2$ essentially also recouples the partial first-order homonuclear dipolar Hamiltonian terms.[14,26] Similar efficiency of suppressing ^{1}H–^{1}H dipolar coupling can be achieved by SR4 and PMRR schemes, as shown in Fig. 1f.

As demonstrated above, the PMRR scheme exhibits superior performance with respect to heteronuclear dipolar recoupling at the ultrafast MAS frequencies. In order to evaluate the versatility of the PMRR recoupling scheme, we have further investigated the recoupling performance of the PMRR scheme at different MAS frequencies from 20 to 120 kHz, which is demonstrated as the tolerance to RF mismatch, resonance offset and homonuclear dipolar couplings at each MAS frequency, as shown in Fig. 1g–i. Not surprisingly, at a higher spinning speed, higher RF field strength is required, which directly leads to higher tolerance to experimental imperfections. When considering RF mismatch in units of percentage rather than kHz, the PMRR performance depends very little on the MAS frequency, as shown in Fig. S2a,† which indicates the robustness to RF inhomogeneity. The effective recoupling bandwidth can also be improved with the increasing MAS frequency, as shown in Fig. 1h. Assuming an allowable accuracy deviation of 10%, the efficient recoupling bandwidth is ±16 kHz at a MAS frequency of 20 kHz, ±50 kHz at a MAS frequency of 60 kHz, and ±100 kHz at a MAS frequency of 120 kHz. The broadband recoupling is rather beneficial for spin systems containing nuclei with a large chemical shift range, such as ^{19}F and ^{31}P. In addition, the capability of suppressing homonuclear dipolar coupling can be further improved with faster MAS frequencies, as shown in Fig. 1i. As a zero-quantum recoupling sequence, PMRR is non-γ-encoded and theoretically sensitive to the fluctuation of spinning frequency, and it is preferable to be strictly synchronized with rotor spinning.[14] Although the increase of the MAS frequency can improve the performance of PMRR, fast MAS also increases the risk of spinning fluctuation that might disrupt the synchronization between pulse irradiation and rotor spinning, leading to performance degradation. However, a fluctuation of ±100 Hz at a MAS rate of 20 kHz yields only an error of less than 0.3% by PMRR, as demonstrated in simulations (Fig. S2b†). For practical MAS NMR experiments, the spinning fluctuation in excess of ±100 Hz should be unusual and attributed to the failure of the MAS control system. Therefore, despite PMRR being non-γ-encoded, the effect of MAS fluctuation is negligible.

Taken together, the above results indicate that the PMRR scheme is a robust heteronuclear recoupling sequence, particularly suited for MAS frequencies of 60 kHz and higher. It is worth noting that, at slow-to-moderate MAS rates, the performance of PMRR might be degraded mostly due to the low

applied RF field, although precise determination can be achieved under specific conditions. Therefore, a more general PMRR scheme with boosted performance suitable for a broad range of MAS frequency is highly desirable.

Windowed phase modulated rotary resonance (wPMRR)

Composite pulses and window insertion are often used to improve the recoupling performance of symmetry sequences.[27,29,42] While composite pulses are suitable for single- and double-quantum recoupling sequences, window insertion is often utilized for zero-quantum recoupling sequences. According to the concept of symmetry sequences, one 4π pulse in PMRR can be regarded as four π pulses in every one rotor period, *i.e.* $R4_1^4$ or $R4_1^0$. Herein, we introduce window insertion into the PMRR scheme, which turns the continuous windowless pulse sequence into one consisting of interval-separated π pulses, dubbed windowed phase modulated rotary resonance (wPMRR). The pulse sequence of wPMRR is shown in Fig. 2a, where the π pulse duration is adjustable. The window fraction, f_w, defined as the ratio of the total interval duration to the rotor periods, was used to represent the pulse characteristics of wPMRR sequences. As f_w is varied from 0 to over 0.9, the recoupling scaling factor increases from 0.50 to over 0.63, as shown in Fig. 2b, where the increase of the scaling factor is more significant in the f_w range from 0 to 0.5. Specifically, the scaling factor of wPMRR is 0.60 for $f_w = 0.5$. At slow-to-moderate MAS frequencies (up to 40 kHz), larger f_w is possible. For instance, $f_w = 0.8$ at 10 kHz MAS requires 100 kHz RF field, which can be accessible on most commercial NMR probes for the ^{1}H channel.

Numerical simulations have been performed to evaluate the robustness of wPMRR at a relatively low MAS frequency (10 kHz), in comparison to the windowless PMRR. As discussed above, the low RF field ($\nu_1 = 2\nu_r$) in windowless PMRR at a lower MAS frequency weakens the recoupling robustness, which would become a challenge for practical applications, especially in spin systems containing nuclei with a large chemical shift range, or with strong homonuclear dipolar couplings. As can be seen from the simulations (Fig. 2c to e), with the introduction of window insertion, the tolerance to the experimental imperfections and spin system is profoundly improved. Therefore, a higher RF field is preferred, as long as the probe hardware permits. At a relatively slow MAS rate of 10 kHz, the robustness of the wPMRR scheme with $f_w = 0.8$ is further demonstrated by comparisons with other commonly used recoupling methods, especially in the suppression of homonuclear dipolar couplings (Fig. S3†). In addition, the introduction of window insertion into the SR4 scheme can also improve the recoupling efficiency as well as the performances. The pulse sequence and performance evaluation of windowed SR4 (wSR4) are shown in Fig. S4.†

In practical applications, multiple interferences may simultaneously come into play, resulting in serious degradation of the dipolar recoupling performance. As illustrated in Fig. 3a, for windowless PMRR at a MAS frequency of 10 kHz, even a slight RF mismatch can significantly deteriorate the performance of ^{1}H–^{1}H dipolar decoupling, making the H–X dipolar measurements unreliable. Similarly, RF mismatch also seriously reduces the performance of suppressing CSA interactions by PMRR, as shown in Fig. 3c, although in principle, the recoupled zero-quantum CSA terms commute with heteronuclear dipolar

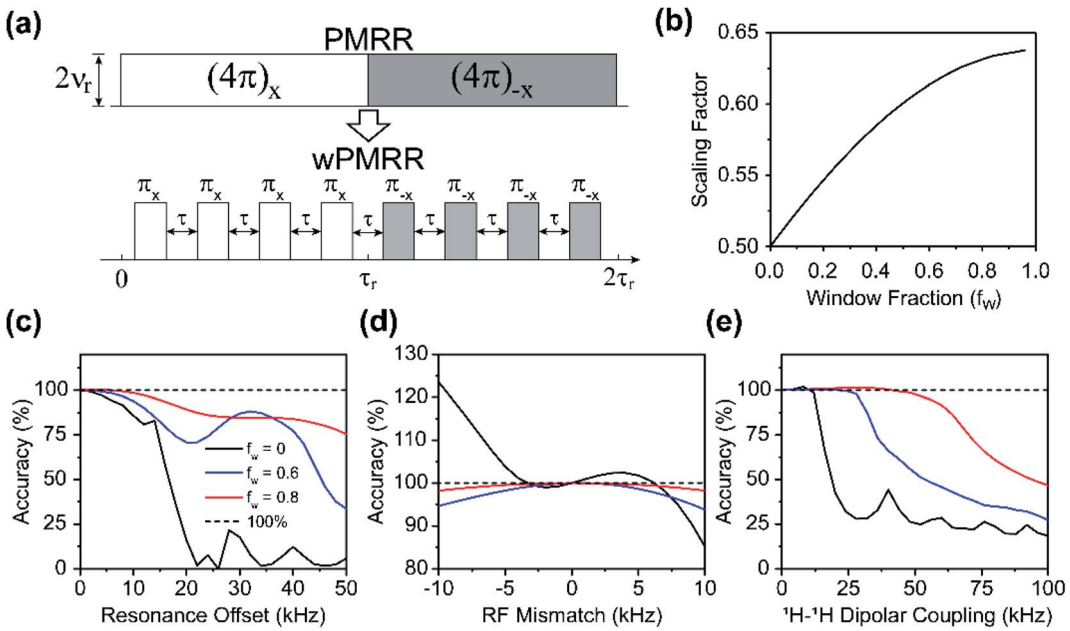

Fig. 2 (a) Schematic diagram of wPMRR. With the introduction of window insertions, the originally continuous 720° irradiation over every one rotor period is transformed into four evenly spaced π pulses. (b) The plot of the recoupling scaling factor of wPMRR as a function of the window fraction varying from 0 to 0.96. The robustness to (c) resonance offset, (d) RF mismatch and (e) ^{1}H–^{1}H dipolar coupling by wPMRR at 14.1 T and a cMAS frequency of 10 kHz, with f_w values of 0 (black), 0.6 (blue), and 0.8 (red), respectively. The dashed lines indicate ideal cases.

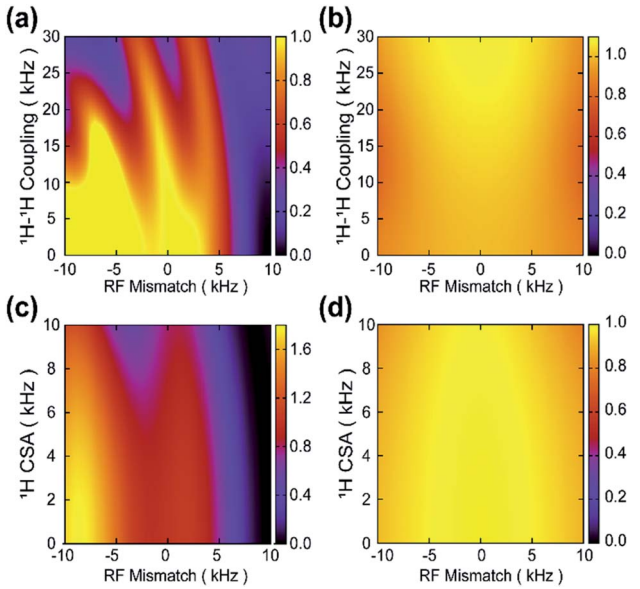

Fig. 3 Simulated plots of the performance of PMRR/wPMRR under two simultaneous interferences; for the magnetic field of 14.10 T and MAS frequency of 10 kHz. The accuracy dependence of $^{1}H-^{15}N$ dipolar measurements by (a) PMRR and (b) wPMRR ($f_w = 0.8$) as a function of RF mismatch and $^{1}H-^{1}H$ coupling. The accuracy dependence of $^{1}H-^{15}N$ dipolar measurements by (c) PMRR and (d) wPMRR ($f_w = 0.8$) as function of RF mismatch and ^{1}H CSA. Each accuracy was evaluated by normalization according to the ideal case.

interactions. And *vice versa*, the tolerance to RF mismatch by windowless PMRR is greatly reduced when the spin system under study contains CSA or/and homonuclear dipolar interactions. However, wPMRR with $f_w = 0.8$ shows significantly reduced dependency on synchronous RF mismatch/$^{1}H-^{1}H$ coupling and RF mismatch/^{1}H CSA, as demonstrated in Fig. 3b and d, respectively. In short, the window modulation makes wPMRR flexible and adaptive to a wide range of spinning frequencies, showing outstanding performance under various conditions. Also, it should be mentioned that the wPMRR scheme makes the experimental setup and optimization greatly simplified, where the only parameter the researcher needs to measure is the π pulse length.

Determination of $^{1}H-^{15}N$, $^{1}H-^{13}C$ and $^{13}C-^{15}N$ DCCs in U–^{13}C, ^{15}N–fMLF

To verify the recoupling performance of PMRR demonstrated above, we have performed $^{1}H-^{15}N$, $^{1}H-^{13}C$ and $^{15}N-^{13}C$ dipolar measurements on U–^{13}C, ^{15}N labelled tripeptide fMLF for two MAS frequencies of 16 kHz and 60 kHz. The 2D PMRR-REDOR and PMRR-DIPSHIFT pulse sequences were used for $^{13}C-^{15}N$ and ^{1}H–X dipolar measurements, respectively. 1D ^{15}N and ^{13}C CP/MAS NMR spectra, as well as the molecular structure and corresponding assignments, are shown in Fig. S5.† $^{13}C-^{15}N$ PMRR-REDOR experiments were carried out at a MAS frequency of 16 kHz, and PMRR irradiation with a RF field strength of 32 kHz was applied on ^{15}N. By observing $^{13}C\alpha$, the directly bonded $^{15}N-^{13}C\alpha$ can be regarded as an isolated spin pair due to the much weaker dipolar interaction with the ^{15}N of the adjacent residue. The $^{15}N-^{13}C\alpha$ DCCs were extracted for each residue by fitting the $\Delta S/S_0$ dipolar dephasing curves, and an example of the experimental and simulated results for Leu is shown in Fig. 4a. 2D PMRR-DIPSHIFT experiments were performed at a MAS frequency of 60 kHz for ^{1}H–X dipolar coupling measurements, where PMRR irradiation with the RF field strength of 120 kHz was applied on ^{1}H. ^{1}H–X DCCs can be obtained by fitting either the dipolar dephasing (free induction decay in the t_1 dimension) or Fourier transformed lineshape. Similarly, ^{1}H–X (X = ^{15}N, ^{13}C) are treated as isolated spin pairs due to the much weaker interaction between the observed X and remote protons. The examples of the experimental/simulated $^{1}H-^{13}C$ and $^{1}H-^{15}N$ dipolar dephasing for Leu are shown in Fig. 4b and c, respectively. In addition, Fig. 4d shows an example of the Fourier transformed $^{1}H-^{15}N$ dipolar lineshape that corresponds to the dipolar dephasing in Fig. 4c. The extracted $^{15}N-^{13}C\alpha$, $^{1}H-^{13}C\alpha$ and $^{1}H-^{15}N$ DCCs for Leu are 908 ± 30 Hz, 22.5 ± 0.3 kHz and 10.7 ± 0.5 kHz, respectively, corresponding to internuclear distances of 1.50 ± 0.02 Å, 1.104 ±

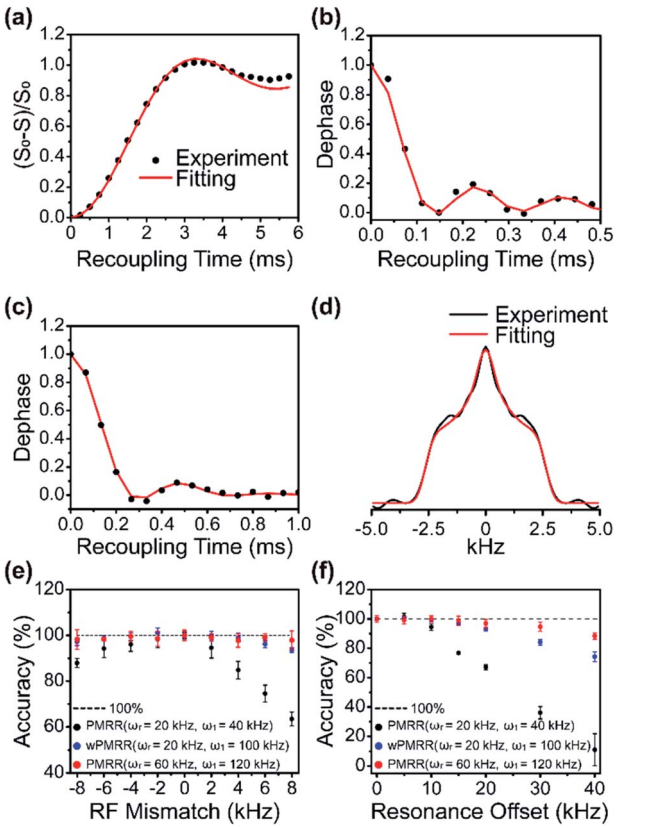

Fig. 4 The experimental (black dot) and fitted (red line) dipolar dephasing curves for the Leu residue in (a) $^{15}N-^{13}C$ PMRR-REDOR, (b) $^{1}H-^{13}C$ PMRR-DIPSHIFT and (c) $^{1}H-^{15}N$ PMRR-DIPSHIFT NMR experiments recorded on U–^{13}C, ^{15}N–fMLF. The MAS frequency was 16 kHz for ^{13}C PMRR-REDOR, and 60 kHz for $^{1}H-^{13}C$ and $^{1}H-^{15}N$ PMRR-DIPSHIFT. (d) The experimental and fitted $^{1}H-^{15}N$ Fourier transformed dipolar lineshapes that correspond to dipolar dephasing free induction decay in (c). The plots of accuracy in $^{1}H-^{15}N$ dipolar measurements by PMRR/wPMRR-DIPSHIFT as a function of RF mismatch (e) and resonance offset (f).

0.005 Å and 1.040 ± 0.005 Å. The experimental and simulated dipolar dephasing curves for each residue are shown in Fig. S6a–c,† and the extracted DCCs as well as the corresponding internuclear distances are indicated in each figure. These results are consistent with the crystalline structure,[43] and also with previous NMR reports.[43] In addition, it should be noted that ^{1}H–X dipolar coupling can also be determined by the PMRR-REDOR scheme. The comparison of the experiment and simulation results for ^{1}H–^{15}N dipolar measurements by PMRR-DIPSHIFT and PMRR-REDOR schemes is shown in Fig. S6c and d,† indicating that the obtained DCCs by PMRR-REDOR are almost identical to those by PMRR-DIPSHIFT.

As demonstrated above, the PMRR scheme is suited for the accurate determination of heteronuclear dipolar couplings in a wide range of MAS frequencies, where interference from both the experimental imperfections and undesired interactions can be suppressed efficiently. The simulation results show that the PMRR scheme is much less sensitive to RF mismatch or inhomogeneity as well as the resonance offset than the original RR scheme, thanks to the effective compensation by the XiX phase modulation. Nevertheless, it is essential to experimentally verify tolerance to pulse imperfections and resonance offset that can accompany practical applications. To do so, we have performed a series of ^{1}H–^{15}N/^{13}C PMRR/wPMRR-DIPSHIFT experiments with varying RF mismatches and resonance offsets on fMLF at MAS frequencies of 20 kHz and 60 kHz. The errors of the dipolar coupling measurements as a function of RF mismatch and resonance offset are shown in Fig. 4e and f, respectively. It is clear that PMRR has superior tolerance to RF mismatch and resonance offset at fast MAS frequencies: very small errors are observed, even with resonance offset up to 40 kHz, consistent with the simulations results. On the other hand, the performance of PMRR degrades at slower MAS frequencies, mainly due to the low RF amplitude ($2\nu_r$) required for the experiments. However, significantly improved performance can be achieved by wPMRR with the RF amplitude of 100 kHz ($f_w = 0.6$) at slower MAS frequencies, which is accessible in most commercial probes, as shown in Fig. 4e and f. More specifically, with wPMRR of $f_w = 0.6$, an RF mismatch of ±8 kHz or resonance offset of up to ±20 kHz results in negligible errors in the measured heteronuclear dipolar constants. Notably, the increasing dipolar scaling factor with increasing RF amplitudes results in faster dipolar oscillation corresponding to broader Fourier transformed lineshapes, as indicated in Fig. S7.† These results demonstrate that the PMRR and wPMRR schemes introduced in this work have excellent tolerance to experimental imperfections and undesired interactions. The robustness to RF mismatch means less stringent requirements for calibration of experimental conditions, the RF homogeneity and stability of NMR probes/amplifiers. Moreover, the good robustness to resonance offset indicates the advantage of broadband recoupling. As mentioned above, in order to maximize the superior robustness for dipolar recoupling, it is recommended to perform PMRR at high MAS frequencies (≥40 kHz) or choose wPMRR with high-power recoupling irradiations for slow-to-moderate MAS frequencies (<40 kHz).

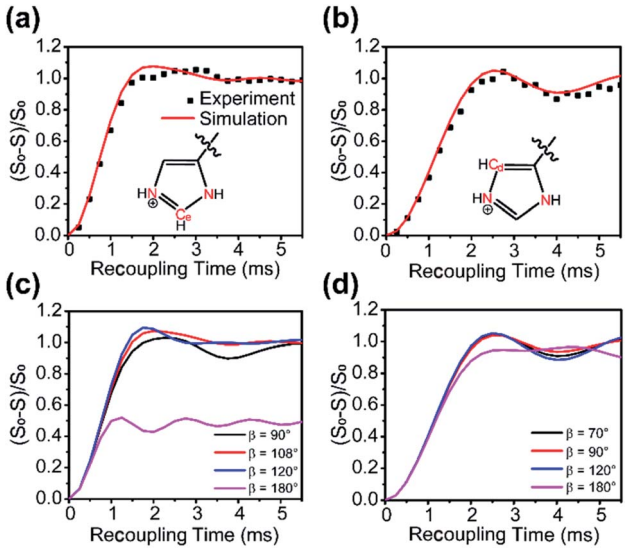

Fig. 5 Dipolar dephasing curves from experiments (black dots) of U–^{13}C, ^{15}N–histidine and simulations (red lines for atoms labelled in red) of the single crystal structure; the acquired signals were ^{13}C. (a) N–C–N angle (β) was 108.7°, the two C–N bond lengths were 1.326 Å and 1.328 Å, corresponding to DCCs of 1302 Hz and 1245 Hz, respectively; (b) N–C–N angle was 69.8°; the two C–N bond lengths were 1.375 Å and 2.201 Å, corresponding to DCCs of 1177 Hz and 287 Hz, respectively; simulations of (c) orientation-dependence of the dipolar dephasing curves, while the ^{13}C–^{15}N distances were set identically to (a); (d) orientation-dependence of the dipolar dephasing curves, while the ^{13}C–^{15}N distances were set identically to (b).

Dependence on geometry of three-spin systems in U–^{13}C, ^{15}N–histidine·H_2O·HCl

In a multi-spin system, heteronuclear dipolar evolution under PMRR is modulated not only by the amplitude of each dipolar coupling, but also by their relative orientations. The analyses of dipolar dephasing curves are able to enrich the geometrical information in the multi-spin system.[14] ^{13}C–^{15}N PMRR-REDOR experiments have been further performed on U–^{13}C, ^{15}N–histidine·H_2O·HCl, where a clear illustration of three-spin systems is ^{15}N–^{13}C–^{15}N in the imidazole ring. When ^{15}N was irradiated by PMRR, the intensity of each ^{13}C signal in the imidazole ring is modulated by two ^{15}N–^{13}C dipolar couplings, as shown in Fig. 5a and b with two representative ^{13}C sites. The experimental ^{13}C–^{15}N dephasing curves for each ^{13}C site agree well with the simulations using the single crystal structure,[44] where an N–C–N angle of 108.7° and two C–N lengths of 1.326 Å and 1.328 Å are for C_ε, while an N–C–N angle of 69.8° and two C–N lengths of 1.375 Å and 2.201 Å are for C_δ. The angles between two ^{15}N–^{13}C dipolar vectors, denoted as β here, have a notable effect on the dipolar dephasing curve. For two ^{15}N–^{13}C dipoles with similar sizes of DCCs, the dephasing curves vary dramatically with different β values (Fig. 5c). However, when the difference of the two DCCs is large, the dephasing curves show less sensitivity to the variation of β (Fig. 5d).

Quantitative probe of the host–guest interaction in zeolites

The ZSM-5 zeolite is well known as a solid acid catalyst which has important industrial applications such as cracking,

alkylation and isomerization.[45–47] The multiple types of acid sites are critical to its catalytic performance.[48,49] Investigation of the acidic nature of H-ZSM-5 can reveal vital details of the catalytic process, and help to manipulate the acidity in ZSM-5 zeolite synthesis and post-synthesis processes. In solid-state NMR, weak bases, such as trimethylphosphine oxide (TMPO), have been mostly used for the characterization of zeolite acidity. TMPO can interact with the Brønsted acid sites (BAS) in the zeolite, and the changes of the chemical environment of both BAS and TMPO make ^{31}P and ^{1}H chemical shifts as probes to characterize the BAS acidity.[48] Over the years, the proximity between BAS and TMPO has been explored qualitatively *via* NMR methods such as ^{1}H–^{31}P HETCOR and HMQC.[48–51] However, there have been few reports on the quantitative studies of the host–guest spatial interaction until now. To obtain the quantitative information of the interaction between zeolite BAS and the adsorbed TMPO molecule, it is necessary to accurately measure the ^{1}H–^{31}P heteronuclear distance, which is significant for understanding the acidic properties of zeolites and revealing more structural details of the adsorbates on zeolite BAS.

The strong proton network from abundant BASs and methyl groups of TMPO is often problematic for the accurate determination of ^{1}H–^{31}P internuclear distances, because the ^{1}H–^{1}H homonuclear dipolar interaction may interfere with the ^{1}H–^{31}P heteronuclear dipolar interaction when conventional recoupling techniques, such as REDOR, are employed.[52,53] As demonstrated above, PMRR and wPMRR sequences can effectively suppress the influence of homonuclear dipolar couplings, and are well suited for heteronuclear dipolar measurements in a broad range of MAS conditions. Considering the detection sensitivity and spectral resolution, a medium-scale 3.2 mm NMR rotor with an accessible moderate MAS frequency was utilized. To achieve the optimum robustness to RF mismatch and resonance offset, we performed wPMRR (f_w = 0.55) NMR experiments for ^{1}H–^{31}P dipolar measurements at a MAS frequency of 20 kHz.

1D ^{31}P MAS and 2D ^{1}H–^{31}P HETCOR NMR spectra are shown in Fig. S8,† and as indicated, in addition to multiple TMPO sites (60–90 ppm) adsorbed on acid sites, the physically adsorbed TMPO with the ^{31}P signal at 46 ppm was also detected.[48,54] Although the saturated adsorption of TMPO was conducted in the preparation, a small amount of BAS was unoccupied by TMPO due to steric hindrance, as suggested by the signal at 4.2 ppm. The signal overlap of protons in TMPO with the BAS proton degrades the ^{1}H spectral resolution, which obscures the direct observation of the ^{1}H signal for tracking ^{1}H–^{31}P dipolar couplings on different BASs, *i.e.*, 2D proton-detected wPMRR-REDOR (Fig. S9a†). On the other hand, 2D heteronuclear ^{31}P-detected PMRR-DIPSHIFT (Fig. S9b†) suffers from the interference of nine protons of methyl groups in TMPO. Therefore, we used a 3D proton-detected wPMRR-REDOR ^{31}P/^{1}H–^{31}P/^{1}H pulse sequence, illustrated in Fig. 6a, for site resolved ^{1}H–^{31}P dipolar measurements with high accuracy. The two CP contacts serve not only for building up ^{1}H–^{31}P correlations for resolving multiple sites, but also as a filter for selecting the proton signals in close proximity to TMPO. The 2D ^{1}H–^{31}P correlation plane sliced from the resulting 3D spectrum at t_2 = 0 is shown in

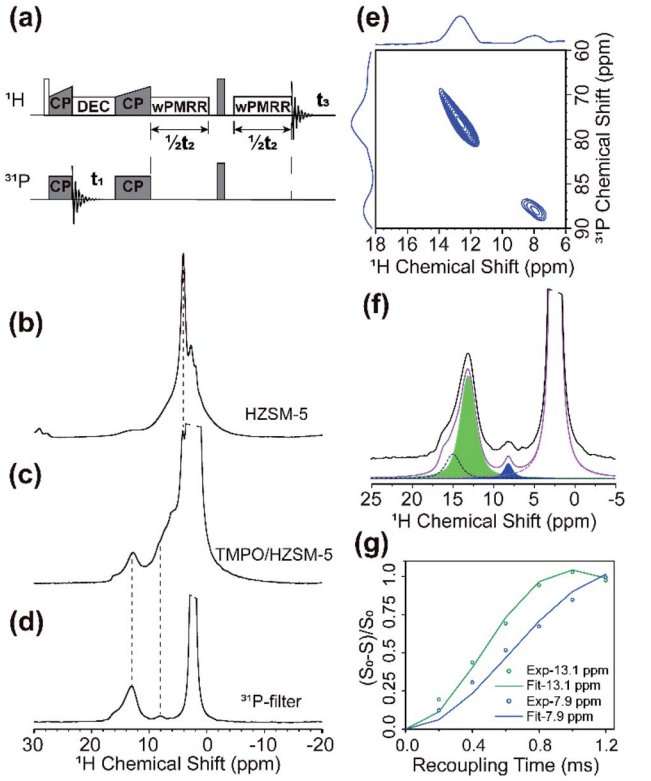

Fig. 6 (a) The 3D ^{31}P/^{1}H–^{31}P/^{1}H sequence. The sequence produced dephasing curve (S), while the T_2 decay (S_0) were recorded by omitting the 180° pulse in the ^{31}P channel. ^{1}H NMR spectra of (b) H-ZSM-5 with SiO_2/Al_2O_3 = 23 after dehydration, labeled as HZSM-5 in the spectra; (c) TMPO/HZSM-5. The cut-off signal belongs to the methyl groups on TMPO; (d) TMPO/HZSM-5 acquired by sequence in (a) with t_1 = 50 μs and t_2 = 0 μs, labeled as the ^{31}P-filter. (e) 2D ^{1}H–^{31}P plane is extracted from the 3D spectrum at t_2 = 0 μs. (f) Deconvolution of (d). Chemical shifts of the three peaks are 14.8, 13.1 and 8.1 ppm. (g) The dephasing curves extracted at 13.1 ppm (green dots) and 8.1 ppm (blue dots), as well as the fitting results in the corresponding color.

Fig. 6e, and two cross-peaks at (13.1 ppm, 78.1 ppm) and (7.9 ppm, 88.1 ppm) are observed unambiguously. The former is assigned to TMPO adsorbed at bridging hydroxyl groups (Si–OH–Al) acting as a Brønsted acid, consistent with previous reports.[48–50,54,55] The latter can be assigned to TMPO adsorbed at BAS with super acidity, *i.e.* the acid is stronger than pure sulfuric acid, as shown by a ^{31}P chemical shift over 86 ppm which was thought to be the threshold of superacidity.[48–51,55]

The ^{1}H NMR spectrum in the direct dimension by 3D wPMRR-REDOR is shown in Fig. 6d; a main signal at 13.1 ppm with a downfield shoulder and a signal at 7.9 ppm correspond to the bridging acid and super acid sites, respectively. The dephasing curves for each site were extracted *via* spectral deconvolution, and one deconvolution example is shown in Fig. 6f. It is noted that the shoulder signal of the main ^{1}H signal can be identified, but the overlap and relatively weak intensity hinder the accurate measurements of the associated dipolar coupling constant. Thus, the data for the shoulder peak are not included. The experimental and simulated ^{1}H–^{31}P dipolar dephasing curves are shown in Fig. 6g. The extracted ^{1}H–^{31}P

DCC for the site at (13.1 ppm, 78.1 ppm) is 2.5 ± 0.2 kHz, corresponding to the internuclear distance of 2.69 ± 0.07 Å, which agrees well with the previous theoretical study.[54,55] In contrast, the super acid site at (7.9 ppm, 88.1 ppm) shows a smaller ^{1}H–^{31}P DCC of 1.8 ± 0.1 kHz which corresponds to a slightly longer internuclear distance of 3.00 ± 0.05 Å. Such adsorption characteristics of the base probe molecule on the super acid sites of H-ZSM-5 suggest that the formation mechanism of the super acid site should be different from the conventional BASs, which may be related to the nearby configurations.

To further investigate the origin of the super acid sites in H-ZSM-5, the TMPO/H-ZSM-5 sample was exposed in a slight humid environment, following the procedure reported previously.[49] As shown in Fig. 7a, the ^{1}H NMR spectrum of the direct dimension in the 3D wPMRR-REDOR experiment indicates that the shoulder peak at 14.8 ppm increases apparently after the rehydration process, with an integral area comparative to the main signal at 13.1 ppm. In the meantime, the ^{1}H signal at 7.9 ppm of the super acid site mostly disappears upon the water adsorption, and the corresponding ^{31}P signal at 88.1 ppm is much reduced as well, as shown in the ^{31}P CP/MAS spectrum (Fig. 7b). As a consequence, the correlation peak at (7.9 ppm, 88.1 ppm) is hardly observed in the 2D ^{1}H–^{31}P correlation plane (Fig. 7c). Several theoretical studies[49,52,56,57] have been reported exploring the origin of the super acidity in H-ZSM-5, and one accepted view is that this is the result of the proximity between the Lewis acid site (LAS) and the BAS.[49,52,57–59] According to the interaction model, it was deduced that the nearby LAS participated in the adsorption of TMPO on BAS, which leads to the super acid sites. Our results reveal that, instead of interacting solely with the acid proton, TMPO interacts with both BAS and LAS, rendering a longer ^{1}H–^{31}P distance on the super acid sites. Fig. 7d shows the experimental and simulated ^{1}H–^{31}P dipolar dephasing curves of rehydrated TMPO/H-ZSM-5 by wPMRR-REDOR. Interestingly, the signal at 14.8 ppm shared the same dipolar dephasing dynamics as the main signal at 13.1 ppm, and the extracted DCCs are 2.6 ± 0.2 kHz (2.59–2.73 Å), which is almost identical to that of the main site at (13.1 ppm, 78.1 ppm) in the as-prepared TMPO/H-ZSM-5. It can be inferred that the high affinity of LAS to H_2O breaks the interaction between TMPO and LAS, which results in the disappearance of the super acid site. The quantitative ^{1}H–^{31}P dipolar measurements by the wPMRR method provide detailed insights into the changes of the TMPO adsorption status on acid sites in zeolites.

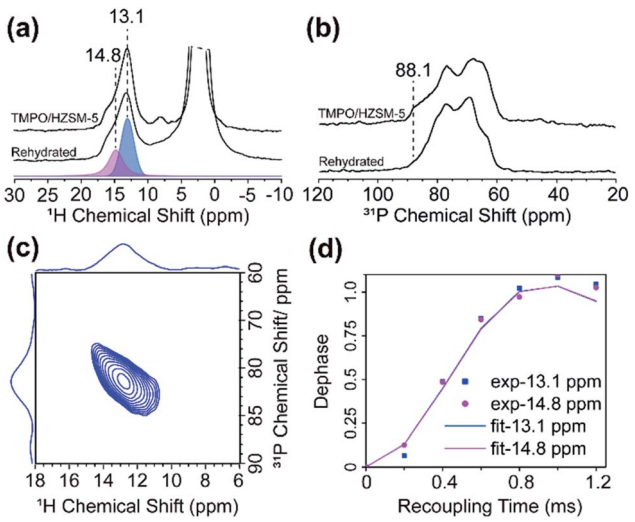

Fig. 7 (a) ^{1}H NMR spectra of as-prepared TMPO/HZSM-5 and after rehydration (labeled as rehydrated), with the deconvolution for the spectrum of the rehydrated sample. (b) ^{31}P CP/MAS NMR spectra of as-prepared TMPO/HZSM-5 and after rehydration. (c) 2D ^{1}H–^{31}P correlation plane in the 3D wPMRR-REDOR experiment of the rehydrated sample. (d) The experimental (dots) and simulated (lines) ^{1}H–^{31}P dipolar dephasing curves extracted for acid sites at 14.8 ppm (purple) and 13.1 ppm (blue).

Conclusions

In summary, a simple and efficient sequence named phase modulated rotary resonance (PMRR) is proposed for recoupling heteronuclear dipolar interactions over a wide range of MAS frequencies. As demonstrated by simulations and experiments, PMRR performs robustly, in comparison to the original rotary resonance and most of the existing recoupling sequences. It shows superior tolerance to RF mismatch and resonance offset while suppressing the CSA and homonuclear dipolar interactions effectively, especially under fast/ultrafast MAS conditions. Although the recoupling performance of windowless PMRR degrades under slow-to-moderate MAS conditions, the modification of window insertion significantly boosted robustness to experimental imperfections and interference from undesired interactions; moreover, the dipolar scaling factor is further improved. It can be concluded that the wPMRR scheme performs better and is highly beneficial for slower MAS conditions. In addition, PMRR allows for the determination of the relative orientation between two interrelated spin pairs.

The outstanding recoupling performance makes PMRR a promising method for measuring the DCC with accuracy and revealing the local chemical structure and dynamics. In probing the host–guest interaction in TMPO adsorbed H-ZSM-5, a proton-detected 3D wPMRR-REDOR pulse sequence has been utilized for determining ^{1}H–^{31}P distances between BAS and TMPO. The results showed unexpectedly longer ^{1}H–^{31}P distances for the super acid site which, in combination with a rehydration experiment, revealed that the super acid site is the result of the synergy of BAS and LAS. The PMRR and wPMRR schemes introduced in this work show superior recoupling performance, excellent tolerance to experimental conditions and imperfections, and more notably, ease of setup. Moreover, it should be noted that PMRR and wPMRR are also suited for determining heteronuclear dipolar coupling between spin-1/2 and spin>1/2, such as ^{1}H–^{17}O and ^{31}P–^{27}Al, where the rotor-synchronized RF field pulses are applied on spin-1/2. Therefore, it is believed that PMRR/wPMRR can find widespread applications in a variety of spin systems.

Author contributions

G. H. conceived the research project, and participated in the experimental design, data analysis, discussion and the revision

of manuscript. L. L. participated in the experimental design, accomplished all simulations, most experimental data acquisitions, all fitting and the data analysis as well as writing of the original draft; Y. J. was responsible for the TMPO@H-ZSM-5 sample preparation; Z. Z. participated in the discussion of experiments and data analysis; C. M. Q. participated in the acquisition of the partial data at 60 kHz MAS; X. H. and X. B. participated in the discussion; T. P. participated in the discussion and the revision of manuscript.

Conflicts of interest

There are no conflicts to declare.

Acknowledgements

We gratefully acknowledge the financial support from the National Natural Science Foundation of China (No. 21773230 and 91945302), LiaoNing Revitalization Talents Program (XLYC1807207), DICP & QIBEBT UN201808, DICP I202104 and the National Institutes of Health of United States (P50GM082251, P30GM103519, and P30GM110758).

References

1 M. Mehring, *Principles of High Resolution NMR in Solids*, Springer-Verlag, Berlin, Heidelberg, 1983.
2 E. R. Andrew, A. Bradbury and R. G. Eades, *Nature*, 1959, **183**, 1802–1803.
3 I. J. Lowe, *Phys. Rev. Lett.*, 1959, **2**, 285–287.
4 E. Brunner, D. Freude, B. C. Gerstein and H. Pfeifer, *J. Magn. Reson.*, 1990, **90**, 90–99.
5 A. Samoson, T. Tuherm and Z. Gan, *Solid State Nucl. Magn. Reson.*, 2001, **20**, 130–136.
6 M. Deschamps, *Annu. Rep. NMR Spectrosc.*, 2014, **81**, 109–144.
7 Y. Nishiyama, *Solid State Nucl. Magn. Reson.*, 2016, **78**, 24–36.
8 M. Schledorn, A. A. Malar, A. Torosyan, S. Penzel, D. Klose, A. Oss, M. L. Org, S. Wang, L. Lecoq, R. Cadalbert, A. Samoson, A. Bockmann and B. H. Meier, *ChemBioChem*, 2020, **21**, 2540–2548.
9 I. Schnell, *Prog. Nucl. Magn. Reson. Spectrosc.*, 2004, **45**, 145–207.
10 G. De Paepe, *Annu. Rev. Phys. Chem.*, 2012, **63**, 661–684.
11 N. C. Nielsen, L. A. Strassø and A. B. Nielsen, in *Solid State NMR*, ed. J. C. C. Chan, Springer, Berlin, Heidelberg, 2012, pp. 1–45.
12 M. H. Levitt, T. G. Oas and R. G. Griffin, *Isr. J. Chem.*, 1988, **28**, 271–282.
13 T. Gullion and J. Schaefer, *J. Magn. Reson.*, 1989, **81**, 196–200.
14 M. H. Levitt, *Symmetry-Based Pulse Sequences in MAS Solid-Sate NMR*, Wiley, New York, 2002.
15 T. G. Oas, R. G. Griffin and M. H. Levitt, *J. Chem. Phys.*, 1988, **89**, 692–695.
16 T. Gullion, in *Modern Magnetic Resonance*, ed. G. A. Webb, Springer, Dordrecht, London, UK, 2008, pp. 713–718.
17 K. T. Mueller, *J. Magn. Reson., Ser. A*, 1995, **113**, 81–93.
18 K. T. Mueller, T. P. Jarvie, D. J. Aurentz and B. W. Roberts, *Chem. Phys. Lett.*, 1995, **242**, 535–542.
19 G. R. Marshall, D. D. Beusen, K. Kociolek, A. S. Redlinski, M. T. Leplawy, Y. Pan and J. Schaefers, *J. Am. Chem. Soc.*, 1990, **112**, 963–966.
20 C. Fernandez, D. P. Lang, J. P. Amoureux and M. Pruski, *J. Am. Chem. Soc.*, 1998, **120**, 2672–2673.
21 M. R. Hansen, R. Graf and H. W. Spiess, *Chem. Rev.*, 2016, **116**, 1272–1308.
22 T. R. Molugu, S. Lee and M. F. Brown, *Chem. Rev.*, 2017, **117**, 12087–12132.
23 J. Schaefer, *J. Magn. Reson.*, 1999, **137**, 272–275.
24 M. Carravetta, M. Eden, A. Brinkmann, X. Zhao and M. H. Levitt, *Chem. Phys. Lett.*, 2000, **321**, 205–215.
25 X. Zhao, M. Edén and M. H. Levitt, *Chem. Phys. Lett.*, 2001, **342**, 353–361.
26 P. K. Madhu, X. Zhao and M. H. Levitt, *Chem. Phys. Lett.*, 2001, **346**, 142–148.
27 M. K. Pandey, M. Malon, A. Ramamoorthy and Y. Nishiyama, *J. Magn. Reson.*, 2015, **250**, 45–54.
28 G. Hou, X. Lu, A. J. Vega and T. Polenova, *J. Chem. Phys.*, 2014, **141**, 104202.
29 X. Lu, H. Zhang, M. Lu, A. J. Vega, G. Hou and T. Polenova, *Phys. Chem. Chem. Phys.*, 2016, **18**, 4035–4044.
30 A. Brinkmann and A. P. M. Kentgens, *J. Am. Chem. Soc.*, 2006, **128**, 14758–14759.
31 L. Chen, X. Lu, Q. Wang, O. Lafon, J. Trebosc, F. Deng and J. P. Amoureux, *J. Magn. Reson.*, 2010, **206**, 269–273.
32 L. Chen, Q. Wang, B. Hu, O. Lafon, J. Trebosc, F. Deng and J. P. Amoureux, *Phys. Chem. Chem. Phys.*, 2010, **12**, 9395–9405.
33 Z. Gan, *J. Magn. Reson.*, 2006, **183**, 235–241.
34 Z. Gan, J. P. Amoureux and J. Trébosc, *Chem. Phys. Lett.*, 2007, **435**, 163–169.
35 G. Hou, I. L. Byeon, J. Ahn, A. M. Gronenborn and T. Polenova, *J. Am. Chem. Soc.*, 2011, **133**, 18646–18655.
36 M. G. Munowitz, R. G. Griffin, G. Bodenhausen and T. H. Huang, *J. Am. Chem. Soc.*, 1981, **103**, 2529–2533.
37 M. G. Jain, G. Rajalakshmi, V. Agarwal, P. K. Madhu and K. R. Mote, *J. Magn. Reson.*, 2019, **308**, 106563.
38 B. Hu, J. Trebosc and J. P. Amoureux, *J. Magn. Reson.*, 2008, **192**, 112–122.
39 M. F. Cobo, D. Reichert, K. Saalwachter and E. R. deAzevedo, *J. Magn. Reson.*, 2014, **248**, 115–125.
40 V. Chevelkov, K. Rehbein, A. Diehl and B. Reif, *Angew. Chem., Int. Ed. Engl.*, 2006, **45**, 3878–3881.
41 B. Reif, *J. Magn. Reson.*, 2012, **216**, 1–12.
42 M. Hohwy, H. J. Jakobsen, M. Edén, M. H. Levitt and N. C. Nielsen, *J. Chem. Phys.*, 1998, **108**, 2686–2694.
43 C. M. Rienstra, L. Tucker-Kellogg, C. P. Jaroniec, M. Hohwy, B. Reif, M. T. McMahon, B. Tidor, T. Lozano-Pérez and R. G. Griffin, *Proc. Natl. Acad. Sci. U. S. A.*, 2002, **99**, 10260–10265.
44 J. Donohue, *Acta Crystallogr.*, 1956, **9**, 655–662.
45 P. Schwach, X. Pan and X. Bao, *Chem. Rev.*, 2017, **117**, 8497–8520.

46 V. Blay, B. Louis, R. Miravalles, T. Yokoi, K. A. Peccatiello, M. Clough and B. Yilmaz, *ACS Catal.*, 2017, **7**, 6542–6566.
47 O. Muraza and A. Galadima, *Ind. Eng. Chem. Res.*, 2014, **53**, 17869–17877.
48 A. Zheng, S. B. Liu and F. Deng, *Chem. Rev.*, 2017, **117**, 12475–12531.
49 S. Xin, Q. Wang, J. Xu, Y. Chu, P. Wang, N. Feng, G. Qi, J. Trébosc, O. Lafon, W. Fan and F. Deng, *Chem. Sci.*, 2019, **10**, 10159–10169.
50 A. Zheng, S. J. Huang, S. B. Liu and F. Deng, *Phys. Chem. Chem. Phys.*, 2011, **13**, 14889–14901.
51 A. Zheng, S. Li, S. B. Liu and F. Deng, *Acc. Chem. Res.*, 2016, **49**, 655–663.
52 K. Chen, M. Abdolrhamani, E. Sheets, J. Freeman, G. Ward and J. L. White, *J. Am. Chem. Soc.*, 2017, **139**, 18698–18704.
53 Z. Yu, S. Li, Q. Wang, A. Zheng, X. Jun, L. Chen and F. Deng, *J. Phys. Chem. C*, 2011, **115**, 22320–22327.
54 A. Zheng, S. J. Huang, W. H. Chen, P. H. Wu, H. L. Zhang, H. K. Lee, L. C. de Ménorval, F. Deng and S. B. Liu, *J. Phys. Chem. A*, 2008, **112**, 7349–7356.
55 A. Zheng, H. Zhang, X. Lu, S. Liu and F. Deng, *J. Phys. Chem. B*, 2008, **112**, 4496–4505.
56 K. Chen, M. Abdolrahmani, S. Horstmeier, T. N. Pham, V. T. Nguyen, M. Zeets, B. Wang, S. Crossley and J. L. White, *ACS Catal.*, 2019, **9**, 6124–6136.
57 S. Schallmoser, T. Ikuno, M. F. Wagenhofer, R. Kolvenbach, G. L. Haller, M. Sanchez-Sanchez and J. A. Lercher, *J. Catal.*, 2014, **316**, 93–102.
58 Y. Chu, X. Yi, C. Li, X. Sun and A. Zheng, *Chem. Sci.*, 2018, **9**, 6470–6479.
59 C. Wang, Y. Chu, J. Xu, Q. Wang, G. Qi, P. Gao, X. Zhou and F. Deng, *Angew. Chem., Int. Ed. Engl.*, 2018, **57**, 10197–10201.